3D printed catalytic converters with enhanced activity for low-temperature methane oxidation in dual-fuel engines

Saeed Hajimirzaee, Aidan M. Doyle*

Department of Natural Sciences, Manchester Metropolitan University, Chester Street, Manchester M1 5GD, United Kingdom;
* corresponding author a.m.doyle@mmu.ac.uk

Abstract

Catalytic converters with non-linear channel structures were prepared using 3D printing and tested in the oxidation of methane in a simulated dual-fuel engine exhaust stream. The design used a simple repeating angular offset between adjacent layers, which was sufficient to introduce complexity with minimal software programming. All 3D printed substrates were mechanically stable and, following washcoating with a composite catalyst, demonstrated higher catalytic activity in methane oxidation than a commercial honeycomb substrate. The methane conversion at e.g. 510 °C was 12.6% on the commercial sample, 72.6% for 90 °, 80.1% for both 30 ° and 45 °, and 89.6 % for the 60 ° oriented structures. This enhancement is attributed to the increased turbulence/mass transfer and surface area than are possible using conventional straight-channelled substrates. Computational fluid dynamics (CFD) analysis confirmed that the higher methane conversion over 3D printed substrates is due (at least partially) to its higher turbulence kinetic energy. Backpressures over the 3D printed structures were also experimentally measured and compared with the conventional honeycomb monolith.

Keywords: dual fuel, methane oxidation, 3D print, additive manufacturing, ceramic, CFD

1. Introduction

Diesel engines are preferred for heavy-duty applications such as domestic and commercial transportation due to their durability, fuel efficiency and higher power density. However, these engines greatly contribute to environmental pollution caused by harmful exhaust emissions[1]. The main pollutants from diesel engines are CO, CO_2, unburnt hydrocarbon, NO_x and particulate matter (PM) which have an adverse effect on the natural environment, land, water, air and, therefore, human health[2]. In 2012, the emissions from diesel engine exhaust were classified as carcinogenic to humans by the International Agency for Research on Cancer (IARC), which is part of the World Health Organization (WHO)[3]. Stricter new regulations on exhaust emission and depletion of fossil fuel resources have forced companies to utilise an alternative fuel and/or technology to overcome this problem. Supplementary fuels such as LNG[4], LPG[5], CNG[6], biogas[7], methanol[8], hydrogen[9], and ammonia[10] have been studied in dual fuel diesel engines, in which LNG and CNG have attracted the greatest attention due to their cost-effectiveness and environmental benefits[11]. Natural gas, which contains mostly methane, is a promising alternative fuel for the transportation sector because it is available at a lower price and produces lower carbon emissions. It has the lowest carbon to hydrogen ratio of any hydrocarbon and, therefore, produces less CO_2 and nearly zero smoke or PM, which is almost impossible in diesel-only engines. Moreover, it significantly reduces the NO_x emission by approximately 50–80%[12]. Other advantages of natural gas include its higher octane number, which means the gas burns hotter and, therefore, can reduce the knocking effect, especially in diesel engines where the compression ratio is relatively high[13]. Furthermore, it has better mixing with air, causing uniform temperature distribution and higher thermal efficiency, which can only be achieved on diesel engines at high loads[14]. However, one of the main drawbacks of using natural gas in dual fuel engines is higher emission of carbon monoxide and unburnt methane from the engine known as "methane slip". This phenomenon is more dominant at low to medium loads. It has been reported that around 90% of the total hydrocarbons (THC) emissions in a CNG/diesel dual fuel engines are unburned methane[6]. The amount of methane emission on a marine vessel with a LNG/diesel dual fuel engines was reported to be around 7 $g.kg^{-1}$ LNG at high load, rising to 23-36 $g.kg^{-1}$ LNG at lower loads.

One practical solution to effectively reduce emission content in the exhaust is to use a catalytic converter. Catalytic converters are made of ceramic or metal substrates coated with active catalysts which are widely used in environmental applications such as three-way catalyst (TWC) for CO and hydrocarbon oxidation and selective reduction of NO_x in small engines; elimination of volatile organic compounds (VOCs) and other organic compounds; hazardous air pollutants (HAPs); and odorous emissions from gaseous effluents[15].

In the auto industry, the common catalyst support for exhaust gas treatment has a monolithic honeycomb structure with a series of parallel tubes and cell density ranging from 300 to 1200 CPSI (cells per square inch). The main reasons that the monolithic honeycomb support is still the first choice for catalyst support in the exhaust after-treatment systems are: available and cost-effective extrusion technology; straightforward washcoating methods; flexibility in cell design; low-pressure drop; and good heat and mass transfer rates [16]. Generally, an ideal monolith with high efficiency should have the following criteria: 1) high surface area to volume ratio; 2) high penetrability with low back pressure; 3) high mechanical strength; 4) low thermal expansion; 4) high-temperature shock resistance; 5) corrosion resistance; 6) chemical inertness[17]. However, having all these properties in one package is extremely challenging, and even the best commercial products cannot meet all these criteria.

Ceramics are the most frequently used materials for manufacturing monolith. Different ceramic materials such as aluminium titanate (Al_2TiO_5), calcium titanate ($CaTiO_3$) and silicon carbide (SiC) have been used[18], yet cordierite, with the chemical composition of $2MgO.2Al_2O_3.5SiO_2$, has become the material of choice owing to its relatively low thermal expansion coefficient and high thermal shock resistance[19].

The channel size and structure of the substrate play an important role in the overall performance. The channels of the most common substrates typically have square, circular or triangular shaped cross-sections that extend in one dimension, similar to a honeycomb structure. These channels provide space for the flow of gases and/or liquids that interact with the active catalyst dispersed on the channel walls via washcoating.[20] Figure 1 shows the relation between wall thickness (w), repeat distance (s), and cell density (N) which is defined as channels per unit of cross-sectional area in inches (CPSI). Other parameters such as open frontal area (OFA) and catalyst loading areas (GSA) can be calculated from w and s.

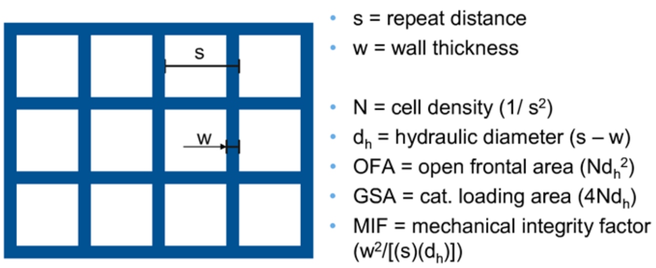

Figure 1. Relation between monolith structural parameters.

Ceramic substrates with CPSI in the range 25-1200 have been manufactured but the most common range for automotive catalytic converter applications is 400-900 CPSI and 0.004 in (0.1 mm) wall thickness[17]. Ultra-thin wall (UTW) ceramic substrates with 900-1200 CPSI and 0.002 in (0.05 mm) wall thickness have been also manufactured and tested. It has been shown that the UTW substrates provide the possibility of reducing the costs of the exhaust system by reducing the amount of precious metals and/or reducing the catalyst volume.

However, these substrates have lower mechanical strength and shorter lifespan due to being more prone to damage[21].

Metallic monolith structures have been manufactured as catalytic converter supports. These substrates can be made with thinner walls and bigger open frontal areas close to 90%, allowing a lower pressure drop. The material used in metallic substrates are commonly ferritic stainless steel alloy with chrome, aluminium and rare earth metals. Typical CPSI values for these metallic monoliths lie in the range 400-600 CPSI with 0.002 in wall thickness[16]. Another advantage of metallic monoliths is their high thermal conductivity and low heat capacity, which allow faster heating during the engine start-up thereby minimising the light-off time[22]. It is also possible to construct the channels with corrugated foils to induce turbulent flow and increase the mass transfer and therefore catalyst efficiency[23]. One of the main disadvantages of metallic monoliths is their higher manufacturing cost. The thermal expansion coefficient is much greater for metallic substrates which means they require special bonding techniques to adhere washcoat onto the metal surface[24].

Another technology that has been developed to improve the efficiency of catalytic converters employs a periodical reversal of gas flow through the catalyst. This technology traps the heat energy from inside the monolith to increase the catalyst operating temperature. This has been used in the purification of industrial off-gases containing VOCs[25]; oxidation of methane and CO emitted from dual LNG dual-fuel diesel engines[26, 27]; NO_x reduction from diesel engines; and emission control during cold start of automotive engines[28]. The main drawback is that the performance of the system strongly depends on the temperature of the exhaust and catalytic reactor. It has been reported that the technology fails to operate efficiently if the reactor temperature or concentrations of HC and CO are too low[27].

Introducing turbulent flow is a promising approach to increase catalytic converter efficiency and/or facilitate a more uniform temperature profile across the catalytic converter[29, 30]. In a conventional extruded monolith, the flow in the frontal section is a jet flow; however it is fully laminar inside the narrow channels,. It is well known that in laminar flow the catalytic reaction is diffusion limited; therefore, different methods have been proposed to increase turbulence in the inlet flow (not inside the channels). One method is to add a device before the monolith to induce turbulence to the gas, prior to entering the channels. Agrawal et al.[31], showed that the turbulence device with a swirl blade configuration is effective in improving the conversion efficiency of the catalytic converter, with lower backpressure relative to other configurations.

Another approach is to create the turbulent flow inside the channels. Figure 2 shows two structures which was proposed by Brük et al. [32], longitudinal structure (LS) and perforated structure (PS). In the LS structure, the monolith is divided into disks that lie perpendicular to the direction of gas flow to generate turbulence on the frontal section of the monolith. Despite having an efficient catalytic converter, the method was not efficient for mass production, due to the high production cost and complicated canning process. In the PS structure, the authors employed corrugated and flat metallic foils containing 8 mm diameters holes to facilitate radial flow inside the channels, which increased conversion and lowered backpressure. However, the differences in thermal expansions between metallic substrates and washcoat have minimised the usage of metal based catalytic converters in original equipment manufacturer (OEM) diesel engines, which makes ceramics the most promising material for such applications.

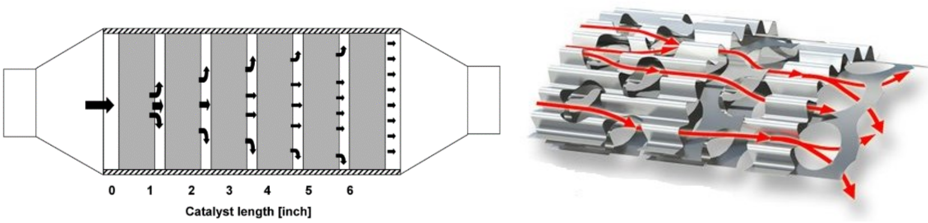

Figure 2 Longitudinal Structure (left) and Perforated Structure (right) for enhanced mass flow in catalytic converter.[32, 33]

3D printing has attracted more attention in recent years as a versatile and low-cost technology for rapid casting/prototyping of a variety of materials, including ceramics.[34, 35] Thanks to its almost unlimited axial flexibility, this technique enables rapid production of customised shapes, the design of which can vary through each of all three spatial dimensions. In the case of catalytic converter substrates, the versatility offered by 3D printing greatly increases the range and complexity of channel structures that are not available using conventional extrusion methods. A number of 3D printing techniques are suitable for ceramics, the choice of which is determined by whether the ceramic material is the form of slurry, powder, bulk solid or paste. Examples of available technologies for 3D printing of ceramics are liquid deposition modelling (LDM); laminated object manufacturing (LOM); for bulk solid/paste materials, stereolithography (SLA); digital light processing (DLP); two-photon polymerisation (TPP); ink-jet printing (IJP); direct ink writing (DIW) and three-dimensional printing (3DP) for slurry based materials; selective laser sintering (SLS); and selective laser melting (SLM) for ceramic powder[36]. Here we report the design and printing of substrate structures with greater complexity than those available in conventional honeycomb arrangements with straight channels and evaluate their performance in the catalytic oxidation of methane.

2. Experimental method

2.1 Substrate 3D printing

Small samples (Ø2.0 cm x H2.0 cm) were printed using cordierite precursors on a WASP 4070 ceramic 3D printer with nozzle diameter 0.7 mm. The technique for deposition of material is LDM (similar to robocasting), which consists of depositing layers of ceramic material (cordierite paste) until the model is formed. Cordierite was synthesised according to a solid-state reaction of cordierite precursors based on a composition available in literature[37, 38]. A paste was prepared by dry mixing of cordierite precursors in powder form according to Table 1, followed by adding water and ethylene glycol (20% of solid weight) with ratio 6:1. The mixture was kneaded until a uniform paste was formed. The paste was then used to print the substrates.

Table 1 Composition of cordierite precursor for solid mixing.

Compound	Talc	Kaolin	Al_2O_3	B_2O_3	Cordierite
Weight (%)	35.4	46.7	12.9	1.7	3.3

Printed samples were dried at room temperature for 24 hours, heated at 1 °C.min^{-1} ramp rate and sintered at 1200 ºC to form the cordierite phase. Subsequently, the substrates were washcoated according to the method described in section 2.2. The weight of washcoat on the substrates was adjusted to be around 0.1 g.

2.2 Catalyst preparation

The catalyst washcoat was chosen to be applicable to auto emission control. The catalyst contained Pd:Pt with 1:1 ratio doped on Al_2O_3/HY zeolite and promoted by cerium, zirconium and titanium oxide. The zeolite used in this formulation was prepared using a geothermal silica source which we previously found to be active in methane oxidation[39]. This activity is attributed to the presence of sodium ions in the structure of the zeolite[40].

The washcoat catalyst was prepared according to the following procedure:

- Support suspension: 1000 mg of support powder was prepared by mixing HY Zeolite, γ-Al_2O_3 (Sigma-Aldrich, activated, neutral), TiO_2 (Millennium PC500), CeO_2 (Sigma-Aldrich, nanopowder <25nm particle size), and ZrO_2 (Sigma-Aldrich, 5µm, 99%) with mass ratio 12:3:3:1:1, respectively. 100ml of water was added to the solid powder and stirred, and the pH was adjusted to 11 by adding NH_4OH solution.

- Precious metal solution: 290 mg $Pd(NO_3)_2.H_2O$ (Alfa Aesar, 99.8%)and 283 mg K_2PtCl_4 (Precious Metals Online, 99 %), were dissolved in distilled water in two separate 50 ml volumetric flasks, followed by ultrasonic treatment for 15 min. Precious metal solution was added dropwise to the support suspension, stirred for 2 hours followed by ultrasonic treatment for 15 min. The resulting suspension was used as washcoat for the substrate. The solid powder was extracted from the catalyst suspension by filtration and converted to pellet form by compression, crushing and finally sieving.
- Both catalyst pellets and washcoated 3D printed substrates were dried at 50 ºC for 24 hours and calcined at 550 ºC for 8 hours.

2.3 Catalyst characterisation

X-ray diffraction (XRD) analysis of powder catalyst was performed at ambient conditions using a Panalytical X'Pert Powder diffractometer with Cu Kα radiation (λ = 1.5406 Å). The diffraction pattern was recorded in the range 5 to 120° with a step size 0.013 and step time 200 s, using an X-ray tube operated at 45 kV and 40 mA with fixed 4° programmable anti-scatter slit. Scanning electron microscopy (SEM) images were recorded using a ZEISS Supra 40VP microscope. Prior to imaging, the samples were sputter-coated with a thin layer of gold. Nitrogen adsorption/desorption measurement was carried out on a Micromeritics ASAP 2020 Surface Analyser at 77 K. Samples were degassed under vacuum ($p < 10^{-5}$ mbar) for 3 hour at 300 °C prior to analysis. BET surface areas were calculated in the relative pressure range 0.05-0.30.

2.4 Catalyst testing

To investigate the effect of structure on substrate performance, washcoated samples were tested under similar conditions in methane oxidation. The feed contains 5 vol.% CH_4, 10 vol.% O_2, 85 vol.% He with GHSV of 400, 800 and 1200 h^{-1}. The weight of catalyst either in pellet form or on the substrate is 0.1 g. When in pellet form, the catalyst was mixed with glass beads, which acted as a diluent to prevent formation of hotspot zones on the catalyst by reducing its activity without affecting the fluid flow through the catalyst bed[41].

2.5 CFD analysis

The effect of structure on fluid dynamics, turbulence and backpressure was analysed using ANSYS Fluent v19.1. The fluid domain was meshed using a tetrahedron method with refined mesh near the walls (Figure 3). Realizable k-epsilon turbulence with default constants were used as a model. Air at room temperature and pressure was used as the fluid and cordierite as the solid material. Boundary conditions are as follow: inlet velocity 0.0066 $m.s^{-1}$ (corresponding to GHSV=1200 h^{-1}), k (turbulent kinetic energy) = 0.0015 $m^2.s^{-2}$, ε (turbulence dissipation rate)=0.00679 $m^2.s^{-3}$, outlet gauge pressure = 0 Pa, temperature = 20 °C. Equations to calculate k and ε are as follows[42]:

$$k = \frac{3}{2}(u_{avg}I)^2 \qquad I = 0.16Re^{-\frac{1}{8}} \qquad \varepsilon = \frac{C_u^{\frac{3}{4}}k^{\frac{3}{2}}}{l} \qquad l = 0.07L$$

where C_u is an empirical constant specified in the turbulence model, which is approximately 0.09, and L is the diameter of the pipe. Number of nodes and elements are listed in Table 2.

Table 2 Number of nodes and elements for different structures

Structure	Number of Nodes	Number of Elements
30 °	1136074	5100584
45 °	1004929	4694231
60 °	1038631	4300399
90 °	1572989	2192526
CPSI 400	248694	1468540

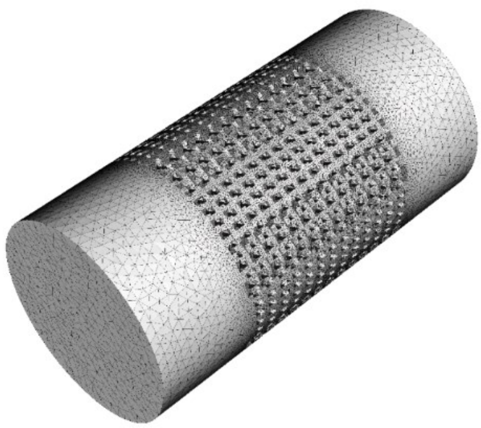

Figure 3. Fluid domain mesh for CFD analysis.

3. Results and discussion

3.1 Ceramic 3D printing

SketchUp was used as the 3D modelling software to design the different structures. The structure is made of layers, which are printed at an offset angle to the preceding layer, and so on, vertically upwards (Figure 4). A conventional honeycomb substrate with straight channels was also designed for comparison purposes. The CAD (computer-aided design) were later used in slicing software to generate the g-code for 3D printing.

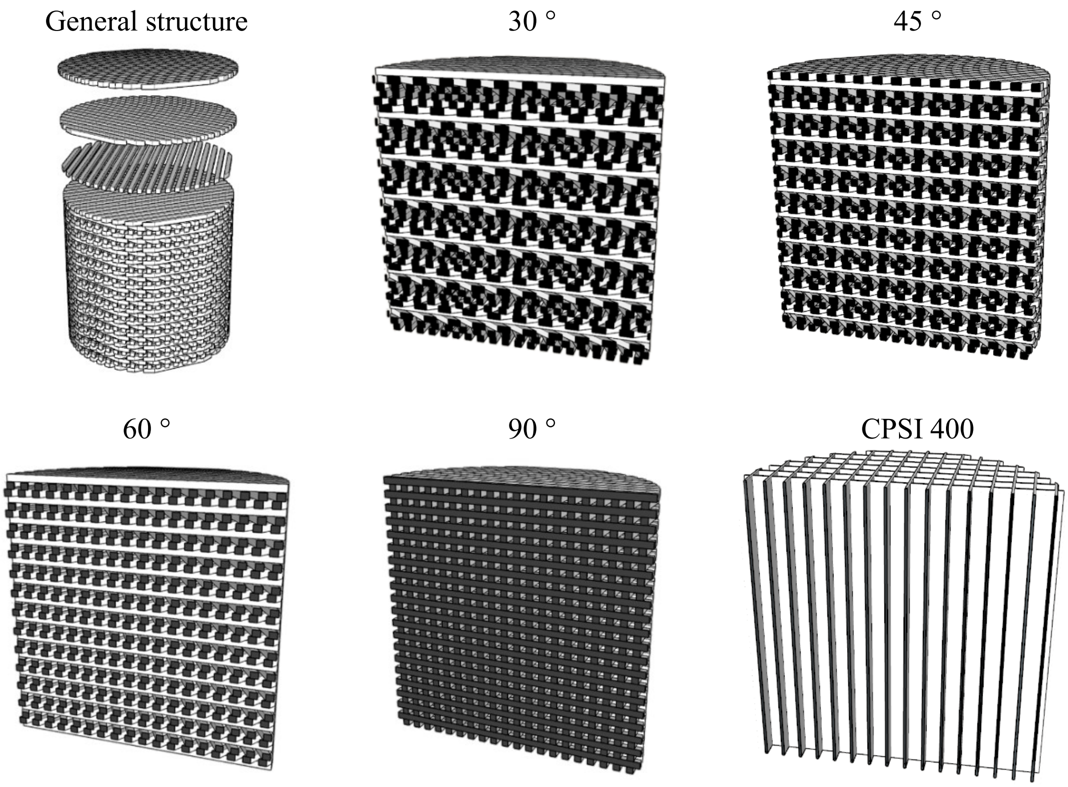

Figure 4. General structure and cross sectional view of 3D printed ceramic substrates.

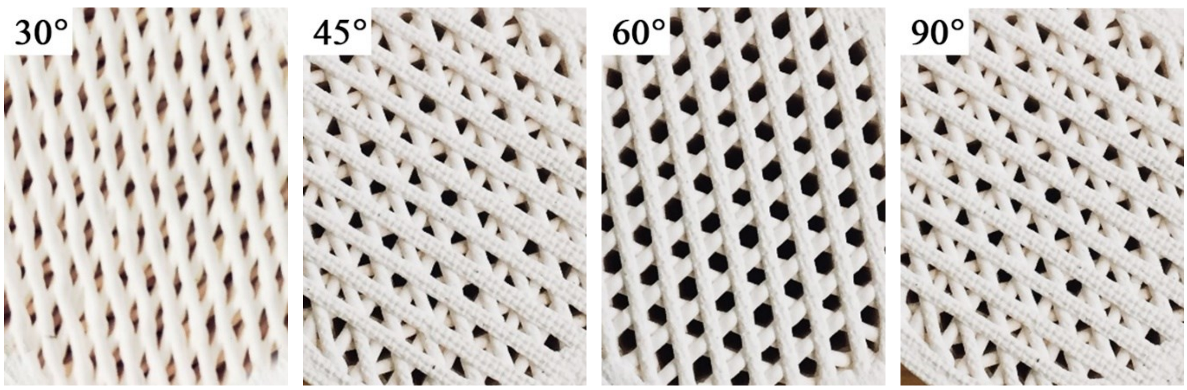

Figure 5 3D printed substrates (Ø2.0 cm x H2.0 cm) with different layer rotation offset (after sintering).

Figure 5 shows optical images of 3D printed substrates with different rotation angles after sintering (but before washcoating). The SEM images of samples after washcoating are shown in Figure 6. Figure 6.a. shows SEM image of substrate with 45 ° offset angle. These samples show less open area, after washcoat, compared to 90 ° (Figure 6.b.) or the commercial sample (Figure 6.c.). Figure 6.d. shows the washcoat in more detail. It should be noted that the 3D printed monolith was prepared with relatively thick walls; this is due to limitations in extrusion of material through the nozzle using the LDM method. From SEM images on Figure 6, this value is around 0.59 mm, equivalent to CPSI 100. The wall thickness for the commercial substrate with CPSI 400 is 0.18 mm which is 70% less than the 3D printed sample.

Honeycomb monolith structures have been manufactured and tested by 3D printing of ceramic material especially cordierite using robocasting or LDM methods[43-45]. Other 3D printing methods such as DLP has shown promising results to manufacture structures with thinner walls and more details. However, material properties (e.g. ceramic particle size and resin formulation) or printing parameters (e.g. layer thickness and exposure time) need to be optimised for a successful print with desirable mechanical properties[46].

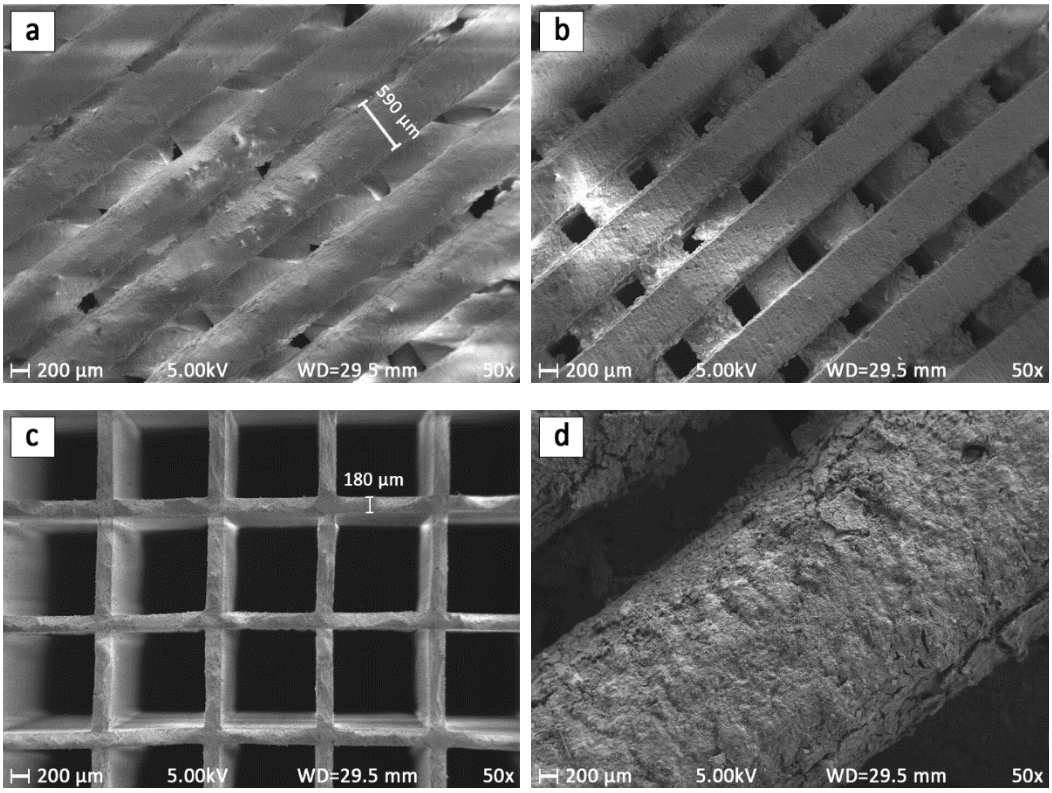

Figure 6 SEM imaging of 3D printed substrates; a) 45 °, b) 90 °, c) commercial, d) catalyst washcoat on substrate.

3.2 Catalyst characterisation

The properties of the fresh and used catalyst support powder, measured by nitrogen adsorption-desorption at 77 K, are listed in Table 3. S_{BET} is the surface area calculated by BET method, V_t is the total pore volume calculated at P/P*=0.98, V_{mes} is the volume of mesopores calculated using BJH method during desorption, V_{mic} is the volume of micro-pores calculated using t-plot method during desorption and d_{BJH} is the average diameter of mesopores calculated using BJH method during desorption. Figure 7 illustrates the adsorption-desorption isotherm of the catalyst washcoat before and after reaction. The graph is consistent with typical type IV adsorption isotherm with H3 hysteresis. Such isotherms are normally for aggregates of plate-like particles that form slit-like pores[47]. Overall, there were slight decreases in porosity characteristics, particularly so for V_{mic} which may have been caused by carbon deposition and/or metal nanoparticles sintering within the micropores.

Table 3 Physical properties of catalyst support powder measured by N_2 adsorption-desorption at 77 K.

	S_{BET} ($m^2.g^{-1}$)	V_t ($m^3.g^{-1}$)	V_{mes} ($m^3.g^{-1}$)	V_{mic} ($m^3.g^{-1}$)	d_{BJH} (nm)
Fresh	363	0.44	0.28	0.16	14.3
Used	311	0.36	0.27	0.09	13.7

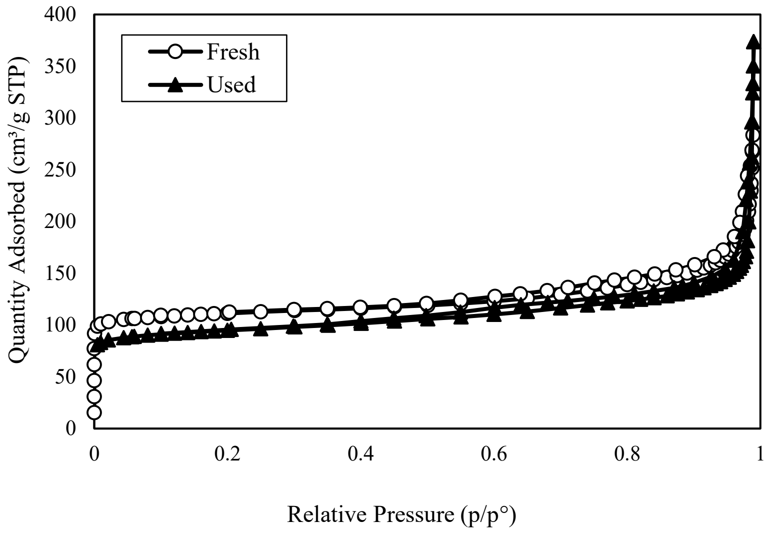

Figure 7 N_2 adsorption/desorption isotherms of fresh and used (TOS = 90 h) catalyst support powder.

Figure 8 shows the the XRD pattern of catalyst washcoat before and after impregnation. The XRD confirms the characteristic crystallinity of Faujasite type zeolite, Al_2O_3, CeO_2 and ZrO_2; the TiO_2 peaks are not visible due to their relatively weak intensities, low concentration of TiO_2 in the overall sample and overlap with other reflections. There was a noticeable decrease in the peak intensities for zeolites. This is due to the partial structural decay of zeolites resulting from the metal impregnation and additional associated calcination step. Moreover, Pd or Pt peaks are not detected due to their low content and implied high dispersion. There was practically no change observed in the *d*–spacing values of the zeolite, which proves that the zeolitic crystalline structure was unchanged after impregnation. Figure 9 shows TEM images of fresh catalyst washcoat and after 90 hours consecutive stability testing. The stability tests were conducted using a reactant stream comparable to an engine exhaust stream, including the presence of steam i.e. 450 °C, 5% CH_4, 20% O_2, 3% CO, 7% CO_2, 6% H_2O, GHSV 1200 h^{-1}). Although slight sintering is observed for only very fine particles, the metal particles size has not been changed significantly. This confirms the catalyst stability against sintering for an extended time.

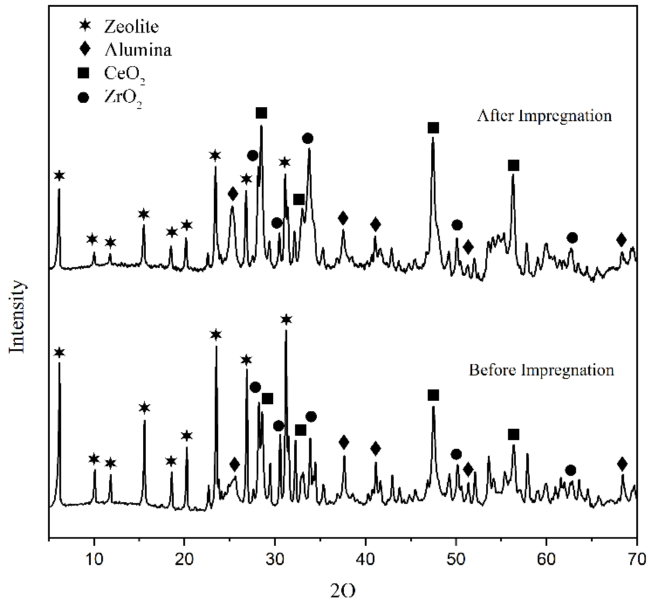

Figure 8 XRD pattern of catalyst support powder, before and after precious metals impregnation.

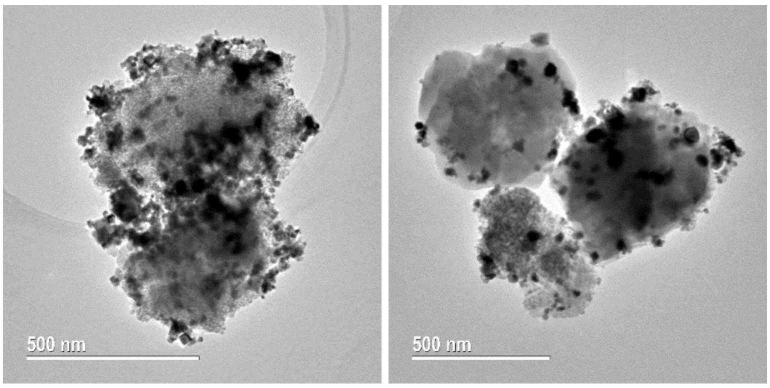

Figure 9. TEM images of catalyst washcoat, a) fresh catalyst (left); after 90 hours stability test (right).

3.3 Methane oxidation

Methane was practically unreactive from 200-250 °C, while the conversions increased continuously thereafter from 250 °C. Figure 10a-c show that the pellets are catalytically active and that no significant change in activity was observed at different GHSVs.

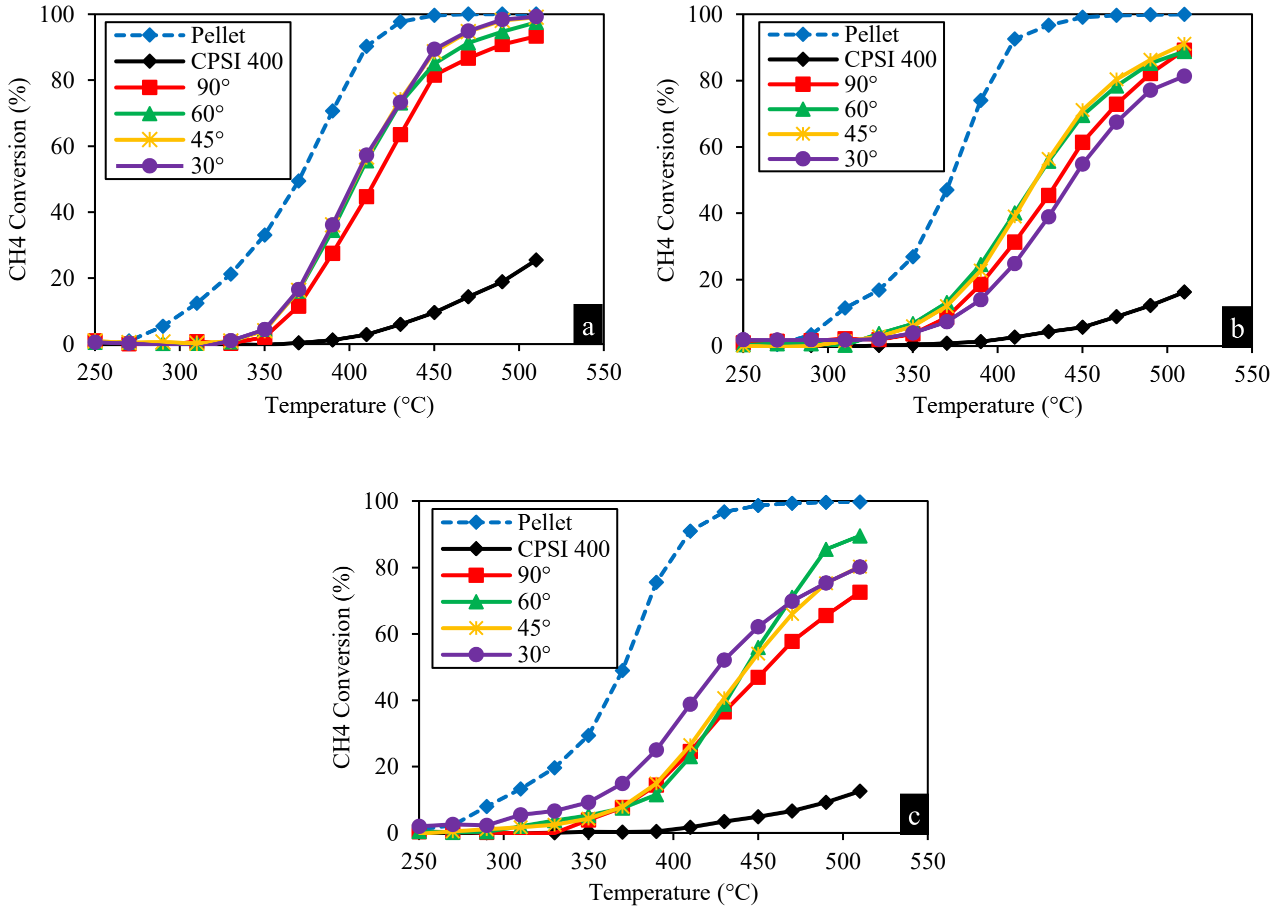

Figure 10 Effect of structure on methane conversion; a) GHSV 400 h^{-1}, b) GHSV 800 h^{-1}, c) GHSV 1200 h^{-1} (CH_4: 5%, O_2: 10%, He: 85%).

All 3D printed substrates showed superior catalytic activity than the conventional CPSI 400 structure. For instance, at 510 °C and GHSV of 1200 h^{-1}, methane conversion is 12.6% on the commercial structure, while this value is 72.6% for the 90 ° structure, 80.1% for both 30 ° and 45 °, and 89.6% for the 60 °. Another interesting observation is the effect of GHSV on performance of 3D printed substrates. At low GHSV (e.g. 400 h^{-1}), all 3D printed substrates have a very similar conversion at temperature range of 350-510 °C, however, increasing the flow rate influenced their catalytic performance. For example, at GHSV of 1200 h^{-1} the 30 ° structure shows better conversion at the temperature range of 300-450 °C, while the 60 ° structure shows the highest conversion at temperatures above 450 °C. At high velocities, the 90 ° structure, which is the most similar in structure to the conventional substrate, shows the lowest activity compared to the other 3D printed structures. In general, these results clearly show that increasing complexity of the channel structure in the 3D printed substrates increases catalytic activity by altering the flow regime and enhancing the mass transfer/turbulence.

Incidentally, the catalyst activity was lower when washcoated on the substrates, relative to pellets, due to the void volume and heat transfer into the substrate, which lowered the overall catalyst temperature.

The increased catalytic activity is also rationalised by the higher surface areas in the 3D printed substrates (Table 4), which result from the unique arrangement of 3-dimensionally oriented layers, thereby exposing a higher proportion of substrate to the external surface. To keep the experimental conditions same, the amount of catalyst loading on the substrate kept similar (e.g. around 0.1 mg).

The preparation of a substrate with lower wall thickness and higher CPSI using more advanced 3D printing technology, e.g. SLA or DLP, will improve the catalytic performance; such trials are currently under investigation by the authors.

Table 4. Relation between structure and physical properties of the substrates (wall thickness of 3D printed substrate = 0.59 mm, wall thickness of commercial substrate = 0.18 mm).

Structure	**Surface Area ($m^2.L^{-1}$)**	**Weight of washcoat (mg)**	**Weight of substrate (mg)**
30 °	3.628	0.104	8.538
45 °	3.633	0.103	8.407
60 °	3.630	0.104	8.286
90 °	3.629	0.095	7.755
CPSI 400	2.876	0.097	2.285

Figure 11 compares the velocity magnitude vectors for both conventional and 3D printed structures. Generally, the 3D printed structure benefits from a higher velocity magnitude and therefore higher turbulence inside the channels. The dark blue colour represents low velocity vectors, which mostly occurs near the walls, while orange and red colours represent high velocity vectors which occurs in the centre of the channels. These regions (orange and red colours) do not exist for commercial substrates and are in the order 30 ° > 45 ° > 60 ° > 90 ° for the 3D printed substrates. Therefore, we tentatively assign the higher conversion of methane over the 30 ° substrate in the temperature range of 300-450 °C to its higher turbulence at this GHSV. It should be noted that the 60 and 90 ° exhibit a lower degree of irregularity compared to 30 ° and 45 °.

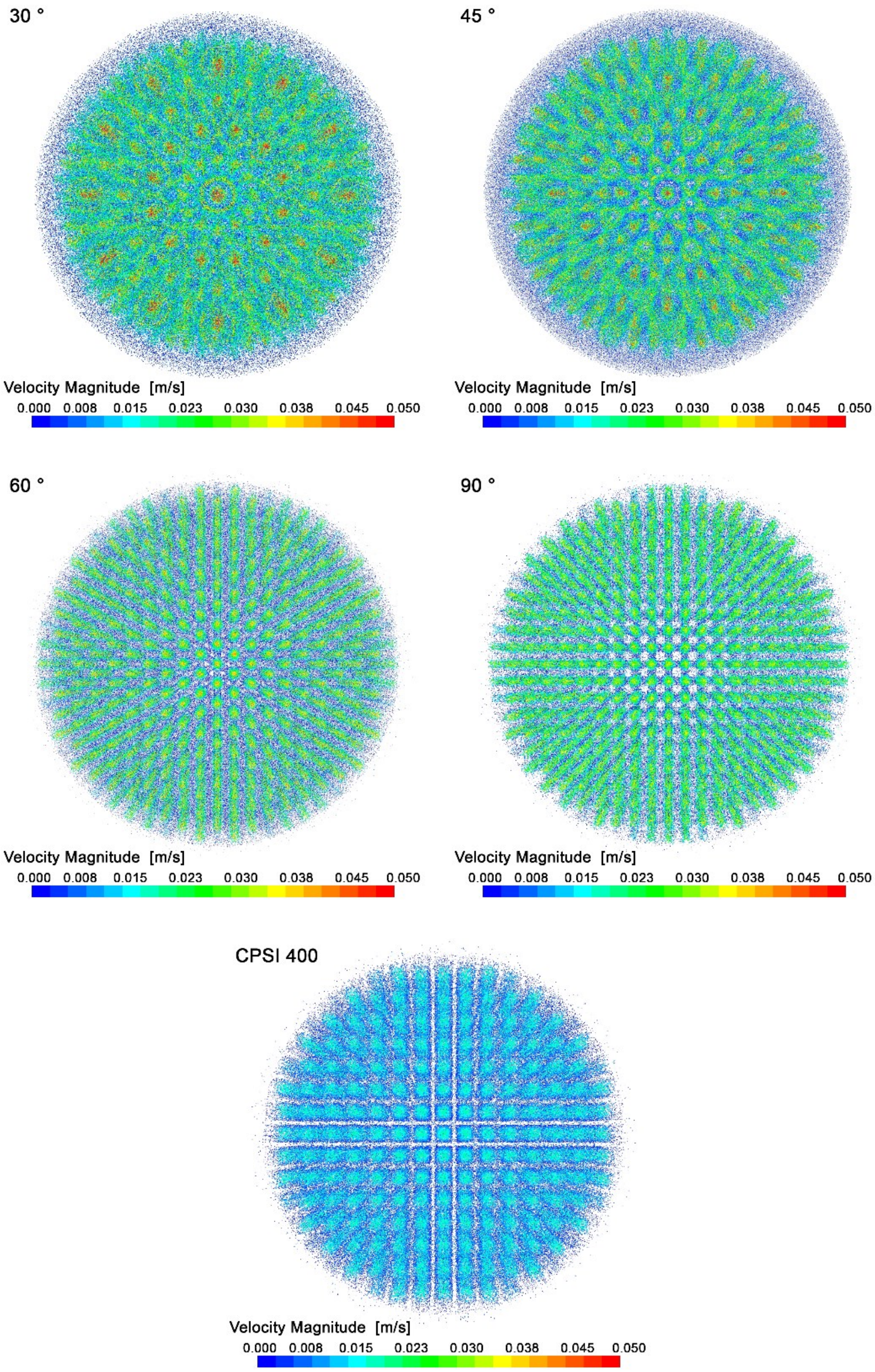

Figure 11. Frontal view of velocity magnitude vectors in the fluid domain for different substrate structures (Fluid: air at 25 °C; GHSV: 1200 h^{-1}).

Turbulent kinetic energy is used to represent the intensity of turbulence in a given region. Figure 12 illustrates the turbulent kinetic energy vector inside the channels across the flow direction. While this value is relatively small (blue colour) and mainly in one direction for the conventional structure, higher turbulent kinetic energy and in different directions is observed for the 3D printed structures. Orange and red vectors are close to the walls, especially where the walls intersect. This is due to the rotation of the wall across the z-axis which leads to the formation of a complex structure. It also can be concluded that the magnitude of turbulent kinetic energy is less for more regular structures (e.g. 60 ° or 90 °). The distribution of turbulent kinetic energy is also more uniform for such structures.

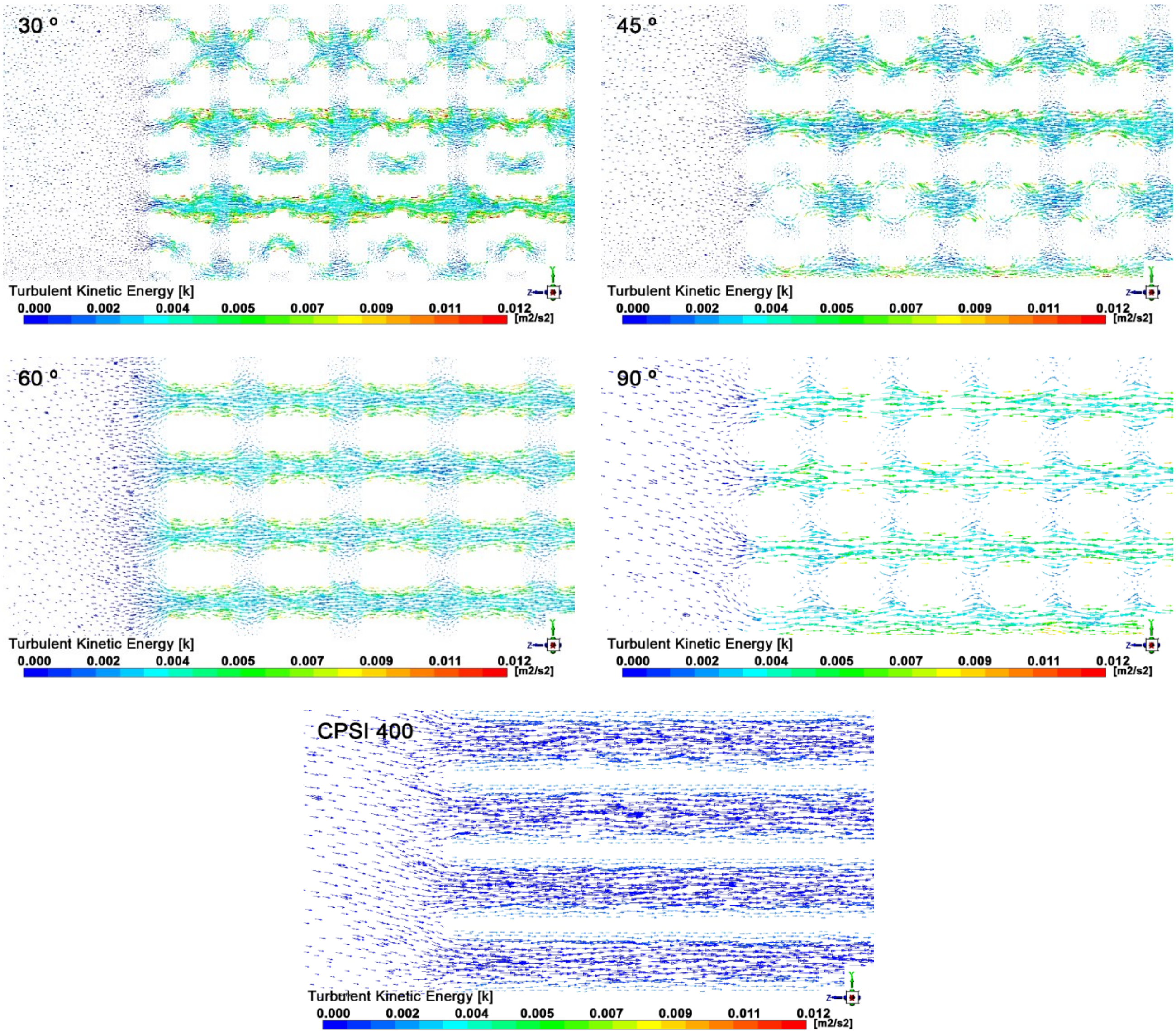

Figure 12. Profile of the turbulent kinetic energy vector inside the channels (GHSV=1200 h^{-1}).

Static pressure profile across the z-axis of substrates is shown in Figure 13. The maximum change in static pressure is observed for the more complex structures, particularly the 30 ° and 45 °, which provide the most turbulence. Pressure drops over 60 ° and 90 ° structures are milder compared to the 30 ° and 45 ° structures but still more than that for the straight-channelled conventional structures.

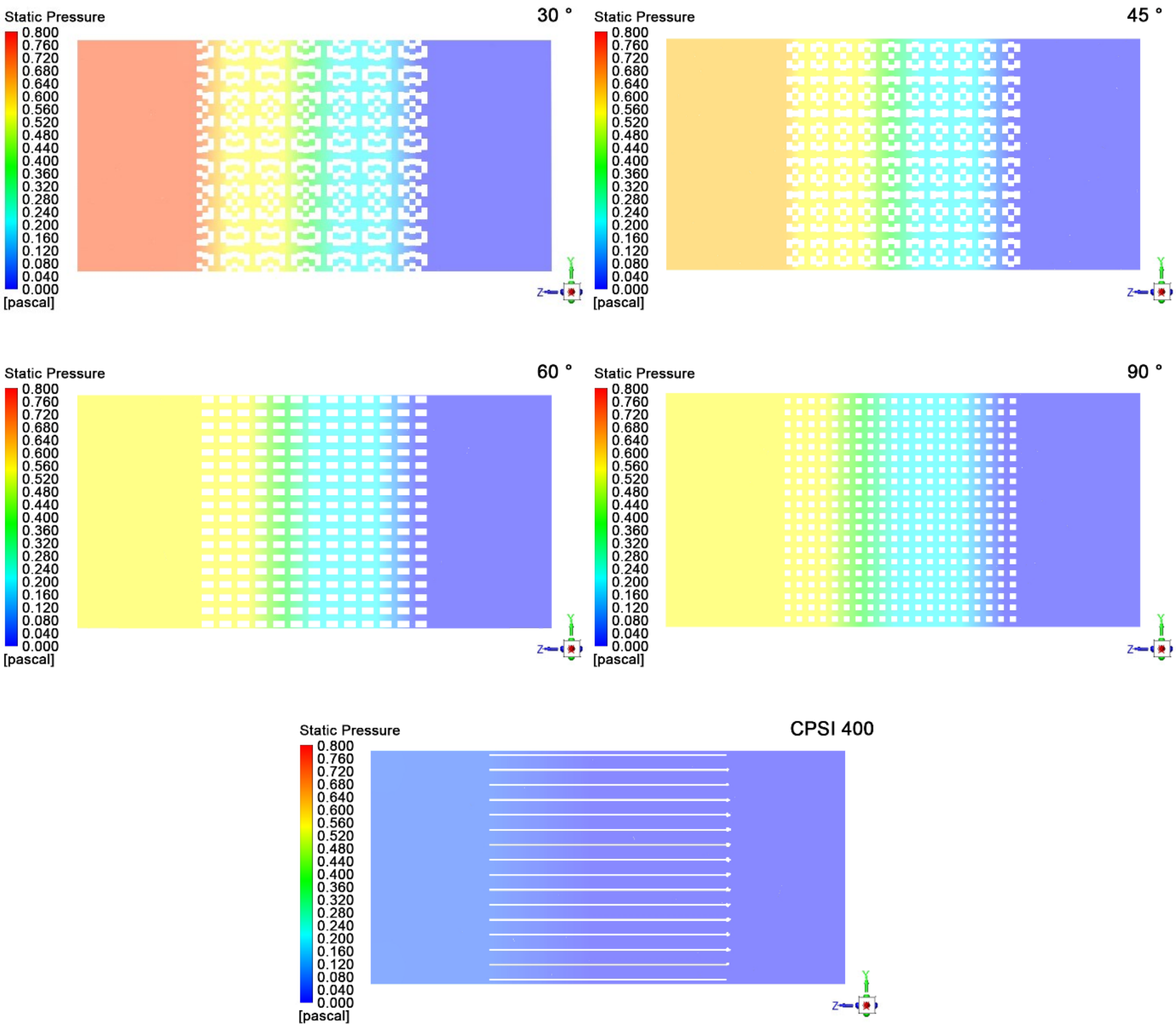

Figure 13 Static pressure profile across the substrate with different structures (GHSV=1200 h^{-1}).

3.4 Backpressure measurement

An experimental method was used to measure the backpressure over different structures at different air inlet velocities. Figure 14 compares the backpressure over different substrate structures for the inlet velocity up to 1.0 $m.s^{-1}$. As expected, the 3D printed structures show higher backpressure compared to the conventional substrates with straight channels. This is due to induced turbulence in these structures, which causes irregular fluctuations and mixing, in contrast to the laminar flow regime with higher velocity inside the straight channels. The backpressure is much less for the structures with more regularity (e.g. 60 ° and 90 °). This is in line with the CFD analysis results where the 30 ° and 45 ° structures exhibited more turbulence.

The highest contribution to backpressure in a real diesel engines is from the diesel particulate filter (DPF) in the after treatment system. The maximum recommended exhaust backpressure by VERT (Verification of Emission Reduction Technologies) for DPF varies. The values are 40 kPa for engines with less than 50 kW power, 20 kPa for 50-500 kW engines and 10 kPa for engines with power more than 500 kW[48]. The results in Figure 14 suggest that backpressure for the 60 ° and 90 ° are close to that for the commercial substrate, which makes these structures suitable for commercial applications.

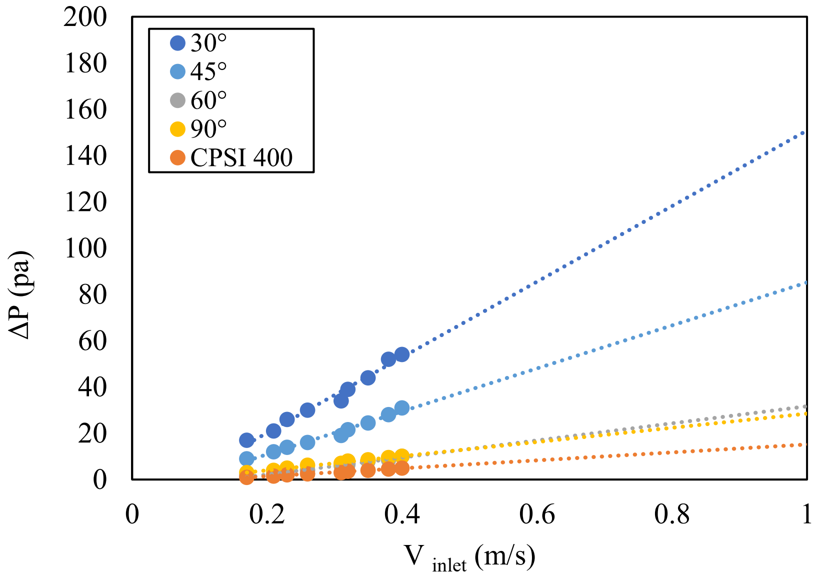

Figure 14 Effect of inlet gas velocity on backpressure over different structures.

4. Conclusions

Catalytic converter substrates prepared by 3D printing of cordierite showed improved catalytic activity in methane oxidation relative to a conventional commercial honeycomb structure. It was shown that the substrates with irregular structures had higher conversion due to the higher turbulent kinetic energy in these structures. The findings provide proof of concept evidence that 3D printing is a suitable means of designing a catalytic converter prototype with higher reaction activity than currently available. The findings have implications for the design and potential mass production of new catalytic materials.

Acknowledgements

This research is funded by an Innovate UK Knowledge Transfer Partnerships (KTP) number 10723 and G-volution Ltd.

References

[1] Reşitoğlu İA, Altinişik K, Keskin A. The pollutant emissions from diesel-engine vehicles and exhaust aftertreatment systems. Clean Technologies and Environmental Policy 2015;17(1):15-27.

[2] Lloyd AC, Cackette TA. Diesel Engines: Environmental Impact and Control. Journal of the Air & Waste Management Association 2001;51(6):809-47.

[3] IARC. DIESEL ENGINE EXHAUST CARCINOGENIC. France: International Agency for Research on Cancer, World Health Organisation; 2012.
[4] Cheenkachorn K, Poompipatpong C, Ho CG. Performance and emissions of a heavy-duty diesel engine fuelled with diesel and LNG (liquid natural gas). Energy 2013;53:52-7.
[5] Saleh HE. Effect of variation in LPG composition on emissions and performance in a dual fuel diesel engine. Fuel 2008;87(13-14):3031-9.
[6] Liu J, Yang F, Wang H, Ouyang M, Hao S. Effects of pilot fuel quantity on the emissions characteristics of a CNG/diesel dual fuel engine with optimized pilot injection timing. Applied Energy 2013;110:201-6.
[7] Nathan SS, Mallikarjuna JM, Ramesh A. An experimental study of the biogas-diesel HCCI mode of engine operation. Energy Conversion and Management 2010;51(7):1347-53.
[8] Wei LJ, Yao CD, Wang QG, Pan W, Han GP. Combustion and emission characteristics of a turbocharged diesel engine using high premixed ratio of methanol and diesel fuel. Fuel 2015;140:156-63.
[9] Saravanan N, Nagarajan G, Sanjay G, Dhanasekaran C, Kalaiselvan KM. Combustion analysis on a DI diesel engine with hydrogen in dual fuel mode. Fuel 2008;87(17-18):3591-9.
[10] Reiter AJ, Kong SC. Combustion and emissions characteristics of compression-ignition engine using dual ammonia-diesel fuel. Fuel 2011;90(1):87-97.
[11] Wei L, Geng P. A review on natural gas/diesel dual fuel combustion, emissions and performance. Fuel Processing Technology 2016;142:264-78.
[12] Abdelaal MM, Hegab AH. Combustion and emission characteristics of a natural gas-fueled diesel engine with EGR. Energy Conversion and Management 2012;64:301-12.
[13] Korakianitis T, Namasivayam AM, Crookes RJ. Natural-gas fueled spark-ignition (SI) and compression-ignition (CI) engine performance and emissions. Progress in Energy and Combustion Science 2011;37(1):89-112.
[14] Ashok B, Denis Ashok S, Ramesh Kumar C. LPG diesel dual fuel engine – A critical review. Alexandria Engineering Journal 2015;54(2):105-26.
[15] Avila P, Montes M, Miró EE. Monolithic reactors for environmental applications: A review on preparation technologies. Chem Eng J 2005;109(1):11-36.
[16] Heck RM, Farrauto RJ. Automobile exhaust catalysts. Applied Catalysis A: General 2001;221(1):443-57.
[17] Williams JL. Monolith structures, materials, properties and uses. Catalysis Today 2001;69(1-4):3-9.
[18] Carty WM, Lednor PW. Monolithic ceramics and heterogeneous catalysts: honeycombs and foams. Current Opinion in Solid State and Materials Science 1996;1(1):88-95.
[19] Liu PS, Chen GF. Chapter Five - Fabricating Porous Ceramics. In: Liu PS, Chen GF, editors. Porous Materials. Boston: Butterworth-Heinemann; 2014, p. 221-302.
[20] Manfe MM, Kulkarni K, Kulkarni A. Industrial application of monolith catalysts/reactors. Int J Adv Eng Res Stud(E-ISSN2249–8974) 2011.
[21] Wiehl J, Vogt CD. Ceramic ultra-thin-wall substrates for modern catalysts. MTZ worldwide 2003;64(2):8-11.
[22] Kašpar J, Fornasiero P, Hickey N. Automotive catalytic converters: current status and some perspectives. Catalysis Today 2003;77(4):419-49.
[23] Müller-Haas K, Rice M. Innovative metallic substrates for exhaust emission challenges for gasoline and diesel engines. SAE Technical Paper; 2005.
[24] Santos H, Costa M. Evaluation of the conversion efficiency of ceramic and metallic three way catalytic converters. Energy Conversion and Management 2008;49(2):291-300.
[25] Bunimovich GA, Strots VO, Matros YS, Mirosh EA. Reversed Flow Converter: Fundamentals of the Design. SAE International; 1999.
[26] Strots VO, Bunimovich GA, Matros YS, Zheng M, Mirosh EA. Novel Catalytic Converter for Natural Gas Powered Diesel Engines. SAE International; 1998.
[27] Liu B, Checkel MD, Hayes RE. Experimental study of a reverse flow catalytic converter for a dual fuel engine. Canadian Journal of Chemical Engineering 2001;79(4):491-506.

[28] Matros YS, Bunimovich GA, Strots VO, Mirosh EA. Reversed flow converter for emission control after automotive engines. Chemical Engineering Science 1999;54(13):2889-98.
[29] Bella G, Rocco V, Maggiore M. A Study of Inlet Flow Distortion Effects on Automotive Catalytic Converters. Journal of Engineering for Gas Turbines and Power 1991;113(3):419-26.
[30] Karvounis E, Assanis DN. The effect of inlet flow distribution on catalytic conversion efficiency. International journal of heat and mass transfer 1993;36(6):1495-504.
[31] Agrawal T, Banerjee VK, Sikarwar BS, Bhandwal M. Optimizing the Performance of Catalytic Convertor Using Turbulence Devices in the Exhaust System. Singapore: Springer Singapore; 2019:333-42.
[32] Brück R, Pace L, Presti M. Turbulent Flow Catalyst: Solution for Euro 5 and beyond. Oct; 2006.
[33] Emitec. Radially open structures (PE-Design®); 2019. Available from: https://www.emitec.com/en/technology/catalyst-substrates/structured-foils/. [Accessed November 2019.
[34] Faes M, Valkenaers H, Vogeler F, Vleugels J, Ferraris E. Extrusion-based 3D Printing of Ceramic Components. Procedia CIRP 2015;28(Supplement C):76-81.
[35] Parra-Cabrera C, Achille C, Kuhn S, Ameloot R. 3D printing in chemical engineering and catalytic technology: structured catalysts, mixers and reactors. Chemical Society Reviews 2018;47(1):209-30.
[36] Chen Z, Li Z, Li J, Liu C, Lao C, Fu Y, et al. 3D printing of ceramics: A review. Journal of the European Ceramic Society 2019;39(4):661-87.
[37] Goren R, Gocmez H, Ozgur C. Synthesis of cordierite powder from talc, diatomite and alumina. Ceramics International 2006;32(4):407-9.
[38] Gonzalez-Velasco J, Gutierrez-Ortiz M, Ferret R, Aranzabal A, Botas J. Synthesis of cordierite monolithic honeycomb by solid state reaction of precursor oxides. Journal of materials Science 1999;34(9).
[39] Doyle AM, Postolache R, Shaw D, Rothon R, Tosheva L. Methane oxidation over zeolite catalysts prepared from geothermal fluids. Microporous and Mesoporous Materials 2019;285:56-60.
[40] Petrov AW, Ferri D, Kröcher O, van Bokhoven JA. Design of Stable Palladium-Based Zeolite Catalysts for Complete Methane Oxidation by Postsynthesis Zeolite Modification. ACS Catalysis 2019;9(3):2303-12.
[41] Bianchi CL, Pirola C, Ragaini V. Choosing the best diluent for a fixed catalytic bed: The case of CO hydrogenation. Catalysis Communications 2006;7(9):669-72.
[42] ANSYS FLUENT User's Guide 12.0. *Using Flow Boundary Conditions.* 2009.
[43] Stuecker JN, Witze PO, Ferrizz RM, Cesarano III J, Miller JE. Revolutionary systems for catalytic combustion and diesel catalytic particulate traps. Sandia National Laboratories; 2004.
[44] San Marchi C, Kouzeli M, Rao R, Lewis JA, Dunand DC. Alumina–aluminum interpenetrating-phase composites with three-dimensional periodic architecture. Scripta Materialia 2003;49(9):861-6.
[45] Mamatha S, Biswas P, Das D, Johnson R. 3D printing of cordierite honeycomb structures and evaluation of compressive strength under quasi-static condition. International Journal of Applied Ceramic Technology 2020;17(1):211-6.
[46] Chen Z, Liu C, Li J, Zhu J, Liu Y, Lao C, et al. Mechanical properties and microstructures of 3D printed bulk cordierite parts. Ceramics International 2019;45(15):19257-67.
[47] Thommes M. Physical Adsorption Characterization of Nanoporous Materials. Chemie Ingenieur Technik 2010;82(7):1059-73.
[48] Mayer A. Number-based emission limits, VERT-DPF-verification procedure and experience with 8000 retrofits. VERT, Switzerland 2004.